Journal of Materials Chemistry A

ROYAL SOCIETY OF CHEMISTRY

PAPER

View Article Online
View Journal

Cite this: DOI: 10.1039/d5ta05950j

Structural and catalytic insights into Pd-UiO-67 frameworks for CO_2 hydrogenation to methanol

Elif Tezel, [a] Beatrice Garetto,[b] Davide Salusso, [c] Dag K. Sannes,[a] Izar Capel Berdiell,[a] Sahra Ahmed,[a] Prantik Sarkar,[de] Stian Svelle, [a] Michael Hirscher, [df] Unni Olsbye, [a] Elisa Borfecchia [b] and Petra Ágota Szilágyi *[a]

This study investigates the catalytic performance of palladium nanoparticles supported on UiO-67, a zirconium-based metal–organic framework (MOF), for CO_2 hydrogenation to methanol, emphasising the influence of the size and location of Pd particles in relation to the MOF matrix. Depending on the synthesis conditions, Pd particles were either supported on the outer surface of the MOF, forming larger nanoparticles (~11–18 nm), or embedded within the MOF pores as smaller particles (~1 nm), with their size constrained by the host framework. Advanced characterisation techniques, including X-ray diffraction (XRD), X-ray absorption spectroscopy (XAS), and transmission electron microscopy (TEM), coupled with catalytic testing, revealed that Pd clusters embedded within the MOF exhibited higher CO_2 conversion and methanol selectivity. This superior performance is attributed not only to the increased surface area-to-volume ratio of the smaller Pd clusters, but also to the enlarged metal–MOF interface, which promotes favourable electronic interactions and enhances the accessibility of active sites. Notably, the confined Pd clusters suppressed methane formation, producing CO as the sole by-product. Despite local distortions at elevated temperatures, the UiO-67 framework maintained its structural integrity under reaction conditions, highlighting its thermal and chemical robustness. These findings deepen the understanding of structure–activity relationships in MOF-based catalysts and underscore the critical role of precise control over metal dispersion and metal-support interfaces in optimising catalytic efficiency and selectivity for CO_2 hydrogenation.

Received 23rd July 2025
Accepted 2nd March 2026

DOI: 10.1039/d5ta05950j

rsc.li/materials-a

Introduction

The escalating global energy demand, driven by rapid population growth and industrialisation, poses a significant challenge due to our continued reliance on fossil fuels. These fuels do not only deplete natural resources but also contribute to severe environmental issues, notably the emission of greenhouse gases such as CO_2 and consequent climate change.[1] Addressing this challenge requires both a transition towards renewable energy sources and advanced technologies for CO_2 utilisation. One promising strategy involves converting CO_2 into value-added chemicals, thereby offering an incentive for reducing its atmospheric concentration through upcycling it into valuable products.[2–5]

Among various CO_2 conversion processes, hydrogenation to methanol is of particular interest due to methanol's potential as a carbon-neutral fuel and as a platform precursor for various high-value chemicals.[6,7] However, achieving high methanol selectivity in CO_2 hydrogenation remains challenging due to different reaction pathways which can co-occur, yielding multiple products, including carbon monoxide, methane, methanol, and higher carbohydrides.[8] Optimal conditions for methanol production typically involve a balance between high temperature and pressure; however, these conditions can lead to reduced selectivity and increased catalyst degradation due to sintering and carbon deposition.[9,10]

To address these challenges, the development of novel catalysts that can achieve high conversion rates and selectivity to methanol under milder reaction conditions is crucial. MOFs present a promising platform for this purpose due to their unique structural properties consisting of inorganic nodes linked by organic ligands, forming highly porous and crystalline structures with high specific surface areas.[11] This porosity could enhance the dispersion of catalytic sites, and improve CO_2

[a]Department of Chemistry, Centre for Materials Science and Nanotechnology, University of Oslo, Norway. E-mail: p.a.szilagyi@kjemi.uio.no
[b]Department of Chemistry, NIS and INSTM Reference Centre, Università di Torino, Turin, Italy
[c]European Synchrotron Radiation Facility, Grenoble, France
[d]Max Planck Institute for Intelligent Systems, Germany
[e]Institute of Separation Science and Technology, Friedrich-Alexander-Universität Erlangen- Nürnberg (FAU), Erlangen, Germany
[f]Advanced Institute for Materials Research (WPI-AIMR), Tohoku University, Aoba-ku, Sendai, Japan

adsorption and activation, potentially allowing for effective CO_2 hydrogenation at lower temperatures.[12] Furthermore, the metal nodes within MOFs can provide Lewis and Brønsted acid sites, which might be instrumental in stabilising key intermediates and facilitating the hydrogenation process.[13]

Recent literature highlights various MOF-based catalysts for CO_2 hydrogenation.[14] For instance, Cu-based MOFs have been extensively studied due to their strong metal-support interactions. An *et al.* demonstrated that Cu/ZnO_x nanoparticles (NPs) supported on UiO-67 MOFs exhibited significantly enhanced catalytic activity and selectivity for methanol production, attributed to the strong interaction between metal-oxo clusters and the Cu/ZnO_x nanoparticles, as well as the confinement effects within the MOF pores.[15] Similarly, Pt-incorporated MOFs have shown promise, with Gutterød *et al.* reporting enhanced methanol selectivity and production rates with Pt nanoparticles embedded in UiO-67, due to the synergistic effects between Pt and the coordinatively unsaturated Zr nodes.[16,17]

In contrast, Pd-based catalysts have also shown potential for CO_2 hydrogenation, but their performance can vary widely, depending on the support and promoter used. Recently, Bugaev *et al.* investigated palladium nanoparticles embedded in UiO-67 to enhance CO_2 conversion.[18] Through the combination of *in situ* X-ray diffraction (XRD) and X-ray Absorption Spectroscopy (XAS) to investigate the catalysts at varying temperatures and pressures they reported the formation of Pd mixed carbide and hydride phases and the adsorption of CO as an intermediate.

Furthermore, thermochemical hydrogenation of CO_2 remains a critical area for research, and understanding the factors that influence reaction selectivity and efficiency is essential for developing effective catalysts. Fine-tuning the intrinsic electronic properties of active metals within MOFs is crucial for optimising catalytic performance.

This study therefore is placed within this context as it is aimed at exploring and optimising the catalytic performance of UiO-67-based composite catalysts incorporating Pd for the hydrogenation of CO_2 to methanol. In contrast to previous works however, we specifically investigated the impact of the nature and location of Pd species in relation to the MOF host, *i.e.* surface-supported or pore-embedded, on the catalytic performance. By systematically analysing the influence of Pd particle size and distribution on CO_2 hydrogenation performance, we aimed to deepen our understanding of structure–activity relationships in MOF-based catalysts. This work would contribute to the design of more efficient catalysts for CO_2 conversion.

Experimental PROCEDURE

Catalyst preparation

The synthesis of UiO-67 was conducted according to a previously reported procedure, with detailed information provided in the SI.[19]

Incorporation of Pd

The synthesised UiO-67 was impregnated with palladium(II) acetate (Sigma-Aldrich) in acetonitrile and stirred continuously overnight. For every 100 mg of UiO-67, 14.6 mg of palladium(II) acetate was used, with a concentration of 10 mg dissolved in 7 mL of acetonitrile. The impregnation process was conducted at two different temperatures: 80 °C and room temperature (25 °C, RT), with the resulting products labelled as Pd-A and Pd-B, respectively. The final products were filtered, washed with acetonitrile, and dried at 80 °C in air overnight.

Characterisation

XRD patterns were collected using a Bruker D8 Discovery diffractometer with Cu K_α radiation (λ = 1.5418 Å). The measurements were conducted on a pressed powder sample holder, covering a 2θ range from 2° to 50°, with a step size of 0.02° s^{-1} under ambient conditions. Nitrogen adsorption isotherms at −196 °C were recorded using a BELSORP mini-II instrument, and the specific surface area of the sample was calculated using the BET (Brunauer–Emmett–Teller) theory. The samples were pre-treated under dynamic vacuum conditions at 80 °C for 1 hour and then at 150 °C for 2 hours prior to analysis. The stability of different samples was analysed using Thermogravimetric Analysis coupled with Differential Scanning Calorimetry (TGA-DSC). TGA was conducted on a Netzsch STA 449 F3-Jupiter instrument. A sample weighing approximately 20 mg was heated from 20 to 900 °C at a rate of 10 °C per minute in an Al_2O_3 sample holder, with a gas flow of 20 mL min^{-1} oxygen and 80 mL min^{-1} nitrogen. The relative quantities of organic species capping the Zr-clusters were quantified using solution-state proton nuclear magnetic resonance (^{1}H-NMR) after dissolving the sample in a 1 M $NaOD/D_2O$ solution. A Hitachi SU8230 field emission scanning electron microscope (FESEM) equipped with an XFlash 6|10 energy-dispersive X-ray (EDX) detector was employed to examine the microstructure and determine the Pd/Zr ratio of the catalysts. Also, the elemental composition of the samples was analysed using an Agilent 4100 Microwave Plasma Atomic Emission Spectroscopy (MP-AES) instrument measuring zirconium at a wavelength of 339.198 nm and palladium at 360.955 nm. Detailed information regarding sample preparation is provided in the SI. HAADF-STEM micrographs were obtained for Pd-A (spent) and Pd-B (spent) using a JEOL ARM300CF operating at 300 kV at ePSIC, at Diamond Light Source. Thermal Desorption Spectroscopy (TDS) spectra were collected using an in-house made apparatus at the Max Planck Institute for Intelligent Systems (MPI IS, Stuttgart, Germany).[20] The details of the apparatus and working principle of the technique is provided in the SI. Approximately 6 mg of each sample was subjected to pre-treatment under vacuum at 150 °C for 2 hours prior to analysis. Following pre-treatment, the samples were exposed to a 50 mbar equimolar mixture of D_2/H_2 isotopes for 30 minutes at RT. Subsequently, the samples were rapidly cooled to 20 K with liquid helium bottles, allowing non-adsorbed gas molecules to be effectively removed under high-vacuum conditions. The temperature was then increased from 20 K to 400 K at a linear heating rate of 0.1 K s^{-1}. Desorbing gas molecules were continuously monitored using a quadrupole mass spectrometer (QMS), which detected

evolved-gas induced pressure increases in the sample chamber corresponding to gas desorption.

In situ XAS/XRD CO_2 hydrogenation experiments were performed at the Swiss-Norwegian beamline BM31 of the European Synchrotron Radiation Facility (ESRF).[21] Approximately 5 mg of the sample was pressed, sieved (125–160 μm), and placed into a quartz capillary (1.5 mm inner diameter, 0.02 mm thickness), with quartz wool plugs at both ends. The capillary was affixed to a custom-designed bracket to allow for gas flow. Heating was provided by a heat blower furnace positioned around the reactor bed. Three mass flow controllers (MFCs), coupled with automated four-way valves, regulated the flows of He (100%), H_2 (10% H_2, balance He), and $CO_2 : H_2 : He$ (1 : 6 : 2). The effluent was analysed using an online mass spectrometer (MS). The measurement protocol is represented in Fig. S16 and briefly consisted in: (I) an initial flushing of the samples with H_2 at room temperature, (II) heating to 170 °C at a rate of 10 °C min^{-1} in H_2 (10% H_2, balance He) and (III) keeping the conditions steady for 1 hour. The H_2 pressure was then raised to 20 bar and (IV) the $CO_2 : H_2$ mixture (20 bar) was then introduced, and the reaction was conducted at 170 °C. (V) The temperature was then increased to 240 °C while pressure was kept 20 bar and (VI) maintained for an additional hour.

XAS data for Zr and Pd K-edges were collected in transmission mode. The beamline was equipped with a water-cooled double-crystal monochromator (Si[111] flat pair), and ionisation chambers filled with a He/Ar mixture were used to measure the incident (I0) and transmitted (I1) photons. XAS spectra were recorded with 1 eV per point energy resolution and 0.1 s per point integration time, for a total acquisition time of approximately 3 minutes per scan per edge. *Ex situ* Zn K- and Pd K-edges XAS spectra were acquired using the same energy resolution and integration time on mass-optimised pellets ($Ø = 13$ mm). The data were energy aligned (to respective metal foils), background subtracted and normalised to a unity edge jump at the respective K-edge using the Athena software from the Demeter suite.[22] *In situ* Pd K-edge XANES spectra were further analysed with Multi-variate Curve Resolution – Alternating Least Square (MCR-ALS) protocol to determine the main spectral species kinetics. Two principal components were identified by Singular Value Decomposition, while SIMPLISMA method[23] was used to determine two independent spectral profiles. The identified spectra were then refined with the MCR-ALS protocol performed using the available Matlab GUI.[24] The spectra profiles were constrained to be positive, the sum of the concentrations was forced to 1 and convergence was determined when 99.98% of the experimental variance was explained.

The experimental setup facilitated automatic switching between XAS and XRD configurations. XRD patterns were obtained following each set of XAS scans, utilising a wavelength of 0.25509 Å and a Dectris Pilatus 2M photon-counting pixel area detector with 30 s acquisition time. The resulting data were azimuthally integrated into one-dimensional powder patterns using SNBL Bubble software, within a 2θ range of 0 to 19.5°. The data were analysed with TOPAS version 6 to determine the scale factors for the two phases-palladium metal and UiO-67. Additionally, the unit cell parameters of the MOF were refined (cubic cell; $Fm\bar{3}m$ space group),[25] with framework atom positions fixed. Thermal parameters were refined in groups with fixed limits, starting with zirconium, followed by carbon, hydrogen, and independently refined oxygen atoms. Gaussian and Lorentzian/Gaussian size broadening parameters were used for MOF and palladium metal phases respectively.

Catalytic testing

Catalytic test results were obtained using a Microactivity Effi (MAE) reactor commercially purchased from PID Eng & Tech and equipped with a silicon-coated stainless-steel fixed bed reactor (inner diameter of 6 mm). The gas chromatograph (GC, Agilent 8890) is installed with three columns: a CP-SIL 8 CB, CS-GasPro (113-4332) and CP molsieve 5A (CP7539). Also, it is consisted of two flame ionisation detectors (FIDs) and one thermal conductivity detector (TCD), and a polyarc was installed prior to one of the FIDs to increase the sensitivity for CO and CO_2. For each experiment carried out in this study, 0.2 g of the catalysts were reduced *in situ* for 4 h at 170 °C in H_2 (10% H_2, balance Ar). Catalytic testing was conducted for 4 hours for each test condition investigated, and all catalytic results were presented as average values. All experiments presented herein were performed using a ratio of 1 : 6 : 2 of $CO_2/H_2/Ar$ and a total flow of 18 mL min^{-1} corresponding to a contact time (τ) of 0.011 g_{cat} min ml^{-1} (STP). The experimental conditions were investigated by consecutively varying the pressure from 1 to 30 bars at 170 °C. After testing the material at 30 bars, the same catalyst was tested again at 20 bars to confirm its stability.

Results & discussion

Catalyst characterisation

Prior to the incorporation of Pd, the crystal structure of pristine UiO-67 was confirmed using X-ray diffraction, ensuring the material's phase purity and crystallinity (Fig. S1.a). The BET surface area was also determined from nitrogen sorption isotherms (Fig. S1.b), yielding a value of approximately 2558 m^2 g^{-1}, which is indicative of a well-synthesised phase-pure metal–organic framework.[26] The sample was further characterised using TGA (Fig. S2.a) and ^{1}H NMR spectroscopy (Fig. S2.b) to precisely determine the ratios of 1,1′-biphenyl-4,4′-dicarboxylic acid (BPDC) and 2,2′-bipyridine-5,5′-dicarboxylic acid (BPYDC) linkers. Theoretical expectations for UiO-67 indicate a composition of 90% BPDC and 10% BPYDC linkers. The BPYDC linker is particularly noteworthy, as literature reports suggest that its bipyridine unit is a preferred site for anchoring metal salts, such as Cu and Pt, within the MOF, and thus presumably Pd.[19,27]

In addition to quantifying the linker ratios, TGA and ^{1}H NMR data were used to assess the extent of missing linker defects, which are crucial as they create additional active sites that enhance the material's catalytic properties.[28] The TGA data was normalised to the residual ZrO_2 content, with the plateau region providing a measure of the overall linker composition. This analysis was complemented by NMR spectroscopy (Fig. S2.b), which offered further insight into the linker distribution and

defect sites. The combined analysis revealed that the amount of missing-linker defects in UiO-67 was approximately 11%, a significant finding as these defects can contribute to improved catalytic activity by generating additional active sites within the framework.[29]

Pd was incorporated into the pristine UiO-67 by varying the incorporation temperature, and the resulting samples were characterised using XRD and SEM. The XRD patterns (Fig. S3.a) confirmed that the incorporation of Pd particles did not affect the crystallinity of UiO-67. Morphological analysis *via* SEM (Fig. S3.b) revealed that possible Pd particles (approximately 10–15 nm) were visible on the surface of the UiO-67 crystallites in the Pd-A sample, which was prepared at an incorporation temperature of 80 °C. In contrast, no Pd particles were observed on the surface of the Pd-B sample (Fig. S3.c), suggesting a distinct difference in Pd deposition behaviour, location and size between the two samples. This difference can be attributed to the effect of incorporation temperature on the diffusion and nucleation behaviour of the Pd precursor within the UiO-67. In the case of Pd-A, prepared at 80 °C, the higher temperature likely accelerates the reduction of the Pd precursor, leading to the formation of Pd clusters before the species can fully diffuse to the bipyridine sites within the UiO-67 framework. These clusters, being larger than the MOF pore size, are consequently deposited on the external surface of the crystallites. In contrast, for Pd-B, prepared at 20 °C, the lower temperature slows the reduction kinetics, allowing sufficient time for the Pd precursor to diffuse through the pore network and coordinate to the bi-pyridine units of the BPYDC linker, which are known anchoring sites for metal ions. This results in the formation of smaller, well-dispersed Pd species predominantly located within the UiO-67 pores. Thus, the incorporation temperature strongly influences both the deposition location and particle size of Pd.

The BET surface area, derived from nitrogen adsorption isotherms (Fig. S4), indicates a value of 2255 $m^2 g^{-1}$ for the Pd-A sample and 2359 $m^2 g^{-1}$ for the Pd-B sample, with the latter closely matching that of the pristine UiO-67 framework. The slight reduction in surface area observed in the Pd incorporated sample could plausibly be attributed to the presence of possible Pd particles, which may partially obstruct the framework's pores and thereby reduce accessible surface area. Another possible reason could be the increased weight of the framework due to Pd incorporation, which might influence the measurement of surface area. However, given that this decrease is around 10%, it is relatively minor and not significant enough to draw definitive conclusions about its cause. Consequently, while the deposition of Pd particles may have minimally impacted pore accessibility, the overall porosity of the UiO-67 framework appears largely preserved in both samples. This minimal variance further suggests that Pd-particle distribution may be either highly dispersed or structured in a manner that limits any significant impact on the surface area. Further compositional analysis of the Pd-A and Pd-B samples using SEM-EDX and MP-AES consistently revealed palladium contents of 5.3 wt% and 5.0 wt%, respectively. These findings indicate that both samples contain comparable amounts of Pd, even though, the distribution and speciation of the Pd differ significantly depending on the incorporation temperature.

To gain understanding regarding the effect of the speciation and size of Pd nanoparticles in the UiO-67 based catalysts on their catalytic performance in CO_2 hydrogenation to methanol, the samples were tested under the same reaction conditions and the results are reported below.

Catalytic CO_2 hydrogenation to methanol

Effect of location and particle size of Pd. To investigate the effect of Pd species' nature on the catalytic performance of UiO-67-based catalysts for CO_2 hydrogenation to methanol, both Pd-incorporated samples were reduced prior to testing under hydrogen (10% H_2, balance Ar) environment. The experiments were performed at 170 °C reaction temperature and under varying pressure ($CO_2/H_2/Ar = 1/6/2$). Each data point reported at a specific pressure was collected for over 4 hours and thus represents the average of multiple measurements. The time-resolved data are provided in SI (Fig. S5 and S6). The results are presented in Fig. 1 and show that an increase in pressure increases both the conversion of CO_2 and methanol selectivity. Also, these results indicate that the Pd-B sample, which contains small Pd clusters presumably confined within the UiO-67, exhibit superior catalytic performance, achieving higher conversions and selectivity at all conditions compared to the Pd-A sample, where larger Pd particles are located on the MOF surface. Specifically, the conversion reported for Pd-B is approximately 40% higher than that of Pd-A in the pressure range of 15–30 bar. Furthermore, the methanol yield is regarded as an informative and practical parameter for evaluating catalytic performance under the investigated conditions. A detailed comparison of methanol yield over the pressure range of 1–30 bar is presented in the SI (Fig. S7). The results show that Pd B consistently exhibits a higher methanol yield than Pd A in the range of 8–30 bar, whereas no methanol formation was detected at 1 bar for either catalyst.

In addition, the experiment was repeated with fresh catalyst for Pd-A to ensure reproducibility, and the results showed negligible differences. These data are provided in the SI (Fig. S8).

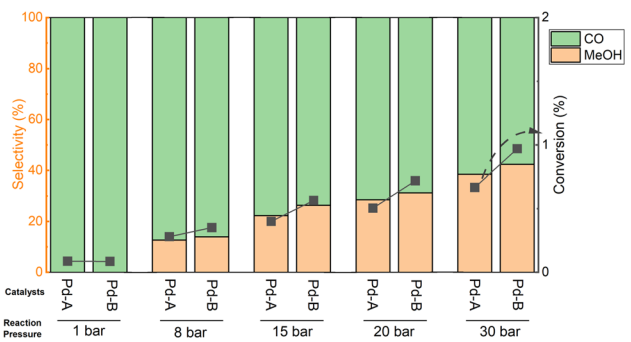

Fig. 1 Product selectivity distribution (left orange axis) and CO_2 conversion (right grey axis) for Pd-A and Pd-B catalysts under varying pressure and at 170 °C ($CO_2/H_2/Ar = 1/6/2$).

Zr_6-based MOF structures with incorporated metal particles have been extensively studied as composite catalysts for CO_2 hydrogenation to methanol.[15–18,29–33] These studies explore various structural, compositional, and reaction parameters to enhance catalytic site dispersion, CO_2 adsorption, and activation, enabling efficient catalysis at lower temperatures. However, the strong interplay between these parameters and catalytic performance, coupled with inconsistent test conditions across studies, complicates direct comparisons with the literature.

Among reported CO_2 hydrogenation catalysts, metal incorporation has been shown to alter the BET surface area, with significant decreases often indicating compromised MOF structural integrity.[14] To contextualise our findings, we compared our results with those from a closely related study by Gutterød *et al.*, who investigated Pt nanoparticles embedded in UiO-67 with mixed linkers (BPDC and BPYDC) under comparable reaction conditions.[16,17] They reported 13% and 40% of methanol selectivities at 170 °C and 8 and 30 bar pressures. Our Pd-B sample achieved slightly higher methanol selectivities of 14% and 43% under similar conditions. Additionally, the Pd-B sample effectively suppressed methane formation, producing only CO as a by-product. This is a desirable outcome, as methane is generally considered a detrimental by-product in CO_2-to-methanol processes due to its tendency to accumulate in the recycle loop, thereby reducing overall process efficiency. In contrast, CO is a valuable intermediate that can be readily recycled into the feed to enhance methanol yield.[34] These results highlight the potential of the Pd-B catalyst in favouring selective methanol production while minimising undesired methanation pathways.

Despite these advantages, CO_2 conversions remained below 2% in both the previously reported study and in our current work, with slightly lower values observed in our study.

Similarly, Bugaev *et al.* investigated palladium nanoparticles embedded in UiO-67 to improve CO_2 conversion.[18] While our study demonstrated superior CO_2 conversion and methanol selectivity compared to their findings, differences in pretreatment and testing conditions prevent a definitive comparison of performance variations to differences in material synthesis.

The superior performance of Pd-B can be attributed to several factors highlighted in the literature. It is well-established that metal clusters and single-atom catalysts confined within MOFs often demonstrate enhanced catalytic activity due to the increased availability of active sites and the unique electronic properties conferred to them by the confinement effect.[35] In the case of Pd-B, the smaller clusters within the UiO-67 framework offer a higher surface area-to-volume ratio and a higher proportion of active surface species, both of which are critical for efficient catalysis. However, it is important to note that this advantage may not extend to all reactions, particularly those that are site-selective, where the specific arrangement of active sites plays a more crucial role than the surface area alone.[36] Furthermore, the electronic effects associated with these catalysts have not been investigated, which may also exert a significant influence on their catalytic behaviour. Studies have shown that such clusters can interact more effectively with CO_2 molecules, facilitating their activation and their subsequent hydrogenation to methanol.[37] Additionally, the nanoconfinement of Pd within the MOF matrix can lead to alterations in the electronic structure of the metal, which can in turn enhance catalytic performance. For instance, the interaction between the metal clusters and organic linkers in the MOF can induce electron transfer processes that stabilise reaction intermediates, thereby lowering the activation energy for the hydrogenation reaction.[38,39] This effect has been observed in other MOF-based catalysts, where the confinement of metal species led to improved activity and selectivity due to the synergistic interaction between the metal and the MOF framework.[29]

In contrast, the Pd-A sample, characterised by apparently larger Pd nanoparticles on the MOF surface, exhibited lower conversion and selectivity. Compared to small clusters, larger nanoparticles offer significantly fewer accessible metal surface area, thereby reducing the likelihood of exposing active catalytic sites per unit of palladium loading. This reduced availability of active sites is evident in the lower conversion rates and selectivity observed (Fig. 1).

The differences in particle size and distribution between Pd-A and Pd-B also likely influence reaction pathways. Smaller Pd clusters within the MOF may favour the formation of methanol over other possible products by stabilising specific intermediates, while larger surface particles might promote alternative reaction pathways, leading to lower selectivity for methanol. This phenomenon is supported by studies on metal-based catalysts, where particle size and distribution have been shown to critically affect product distribution in CO_2 hydrogenation reactions.[34,40,41] These findings highlight the critical importance of controlling the size, distribution, and location of Pd species within the MOF structure to achieve optimal catalytic performance. Notably, the formation of Pd clusters within the MOF, as observed in Pd-B, enhances both conversion and methanol selectivity in CO_2 hydrogenation. This suggests that precise engineering of Pd incorporation can play a pivotal role in tailoring the catalytic behaviour for desired outcomes. Furthermore, although the reaction in Pd-B occurs within the MOF pores, we note that internal mass transport limitations were not explicitly measured in this study; nonetheless, the pore architecture of UiO-67 likely facilitates efficient reactant diffusion and product evacuation under the reported catalytic conditions. While a detailed mechanistic investigation is beyond the scope of this study, the analogous incorporation of Pd nanoparticles within the UiO-67 framework to the Pt⊂UiO-67 system suggests that similar interfacial effects may underlie the observed methanol selectivity.[41]

Following the reaction, both XRD and SEM analyses were performed on the Pd-A(spent) and Pd-B(spent) samples. The XRD diffractograms and SEM images, presented in Fig. S9 and S10, revealed no significant changes in either the crystal structure or the morphology of the samples. However, while a slight increase in the BET surface area was observed (Fig. S11), with values of 2515 $m^2\ g^{-1}$ for Pd-B sample, almost no change (2272 $m^2\ g^{-1}$) was observed for Pd-A sample. Also, after testing the material at 30 bars, the same catalyst was re-tested at 20 bars to

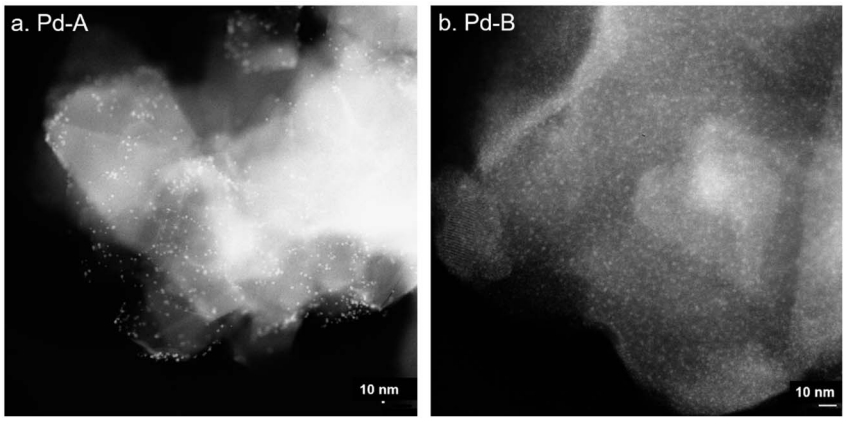

Fig. 2 HAADF-STEM micrographs of a. Pd-A and b. Pd-B after activation followed by CO_2 hydrogenation reaction.

confirm its stability. A minor decrease in selectivity towards methanol was observed, while no reduction in CO_2 conversion was noted for either catalyst (Fig. S12).

Furthermore, TEM images of the Pd-A and Pd-B samples after activation at 170 °C for 4 hours, followed by CO_2 hydrogenation testing at 170 °C for approximately 20 hours, are shown in Fig. 2. In the Pd-A sample, the Pd NPs, sized between 11 and 18 nm in diameter, are located on the surface of the UiO-67 framework. In contrast, the Pd-B sample exhibits very well-distributed Pd NPs within the UiO-67 structure, with an average particle size of approximately 1 nm. Since the images were taken after the reaction, the results indicate that no significant agglomeration occurred, although slight particle growth cannot be entirely ruled out. The Pd-B sample maintains a uniform dispersion of Pd NPs within the MOF, highlighting the material's stability under reaction conditions.

On the other hand, the *ex situ* Pd K-edge XANES (Fig. 3a) and FT-EXAFS (Fig. 3b) spectra of the two Pd-functionalised MOFs, analysed in their as-prepared (pristine) and post-catalytic (spent) states, revealed key details into the Pd oxidation state and local coordination environment. In its pristine state, the Pd-A samples exhibited a significantly lower white-line (WL) peak intensity and a subtle shift of the rising edge towards lower energy values compared to Pd-B in the XANES region. This shift indicated a partial reduction of Pd in the Pd-A sample, suggesting that the palladium already existed in a more reduced state in Pd-A compared to Pd-B while in their pristine states. The broad WL features observed in both Pd-A and Pd-B were consistent with locally disordered structures, resembling those typical of palladium acetate. In contrast, the sharper and more distinct WL characteristics of PdO were absent, suggesting that palladium in both samples did not form well-defined agglomerates after synthesis.[42–44]

Complementary analysis using FT-EXAFS supported these observations, identifying a Pd–O coordination peak in both samples, indicative of oxidised Pd species resembling the Pd(II) acetate precursors. The coordination environment of the Pd-B sample closely resembles that of Pd(II) acetate. However, the complexity of the local coordination environment around palladium leads to low-intensity high-*R* features, making it

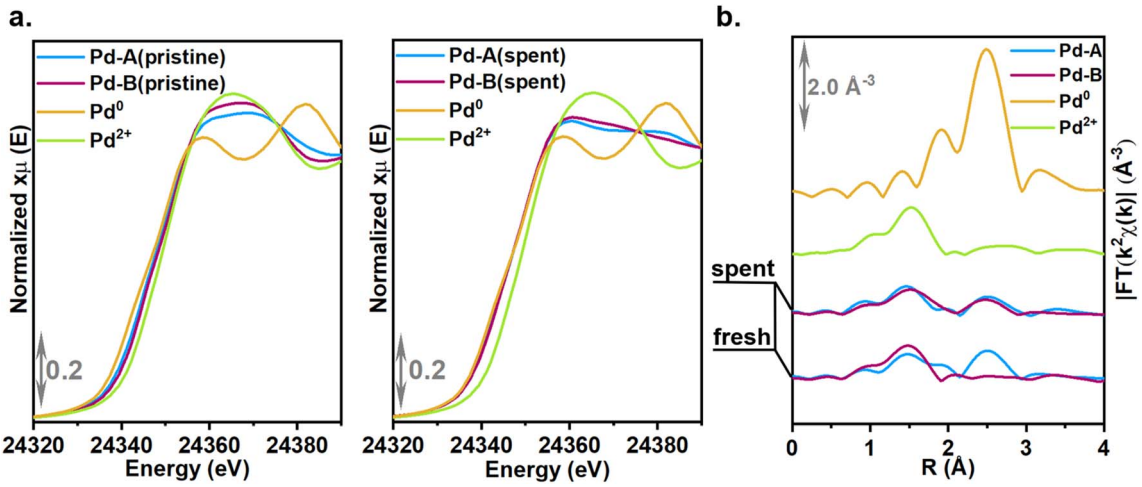

Fig. 3 (a) *Ex situ* Pd K-edge XANES spectra comparing between Pd-A and Pd-B samples in their pristine (left) and spent (right) forms, alongside spectra of relevant model compounds: Pd(II) acetate (Pd^{2+}) and Pd metal foil (Pd^0). (b) Corresponding phase uncorrected magnitude component of FT-EXAFS spectra, obtained by Fourier transforming the $k^2\chi(k)$ curves in the 2.7–12.0 $Å^{-1}$ range. Experimental EXAFS spectra are provided in Fig. S17.

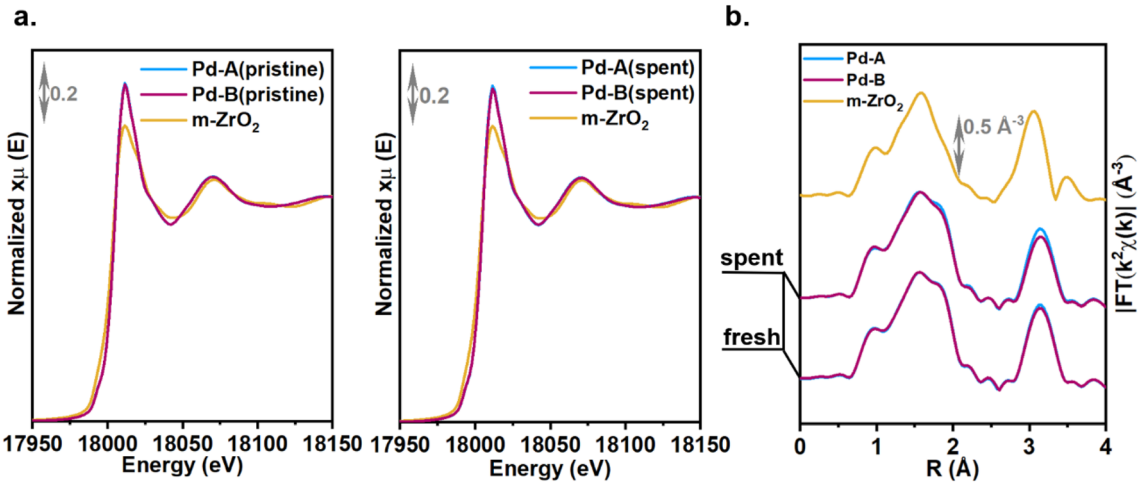

Fig. 4 (a) *Ex situ* Zr K-edge XANES spectra comparing between Pd-A and Pd-B samples in their pristine (left) and spent (right) forms, alongside the spectrum of a ZrO_2 reference for comparison. (b) Corresponding phase uncorrected magnitude component of FT-EXAFS spectra, obtained by Fourier transforming the $k^2\chi(k)$ curves in the 2.4–15.0 $Å^{-1}$ range. Experimental EXAFS spectra are provided in Fig. S18.

difficult to clearly identify Pd-bpy species.[45] In contrast, Pd-A exhibited a pronounced peak at approximately 2.5 Å in the phase-uncorrected FT-EXAFS spectra, corresponding to the Pd–Pd single scattering signal and indicating the presence of metallic palladium. These findings strongly suggested that, while both samples exhibited a Pd(II) state, Pd-A uniquely contained partially reduced palladium nanoparticles. This analysis supports the hypothesis that Pd-A contains large, partially reduced Pd nanoparticles, as suggested by SEM observations, while also revealing that these metallic nanoparticles are preferentially located on the surface of the MOF crystallites. This positioning, coupled with their larger size due to the absence of confinement effects within the MOF pores, likely contributed to the lower conversion and methanol selectivity observed for Pd-A (see Fig. 1).

Post-experiment analysis revealed the presence of a Pd–Pd peak in the EXAFS spectra, confirming that the formation of Pd nanoparticles was an irreversible process. Furthermore, the persistence of the Pd–O coordination peak with comparable intensity in both samples suggested that the observed small differences in the intensity of the Pd–Pd peak could be attributed to variations in the dimensions of the Pd nanoparticles, which were more prominent in Pd-A compared to Pd B (see in Fig. 6b, the peaks located at 2.5 Å phase-uncorrected).

Concerning the *ex situ* Zr K-edge results, the XANES spectra (Fig. 4a) closely matched the monoclinic ZrO_2 reference (m-ZrO_2). The presence of a 1s → 4d pre-edge transition, characteristic of local non-centrosymmetric Zr–O coordination,[46–50] and a more intense white-line compared to m-ZrO_2 were consistent with literature spectra of UiO-66(Zr).[51] These observations confirmed the persistence of a Zr^{4+} oxidation state under all examined conditions, with no detectable changes before or after the catalytic reactions. This spectral consistency was further supported by the EXAFS results (Fig. 4b), where the second-shell peak attributed to Zr–Zr scattering was consistently observed across all samples. These findings demonstrated that the structural integrity of the MOF matrix was maintained throughout the experiments for both samples. This conclusion was corroborated by the stability, evident in the PXRD and SEM results (see Fig. S9 and S10).

TDS experiments were conducted to investigate the desorption behaviour of hydrogen from UiO-67, both with and without Pd incorporation, focussing on differences between reduced samples (following hydrogen pretreatment but prior to catalytic reactions) and spent samples (post-catalytic reactions). The reduced and spent Pd-A and Pd-B samples were exposed to a 50 mbar 1 : 1 H_2/D_2 isotope mixture RT, and the resulting desorption spectra are presented in Fig. 5 and S9–11. The HD desorption data is specifically highlighted to compare reduced and spent samples and identify characteristic spectral peaks. Comprehensive thermal desorption spectra for both H_2 and D_2 in Pd-functionalised and unmodified UiO-67 frameworks are provided in the SI (Fig. S13–15).

Characteristic low-temperature desorption peaks observed across all samples include a signal below 50 K attributed to condensed H_2 within the pores of the framework. Desorption signals between 50 K and 125 K correspond to hydrogen release from specific binding sites within the MOF, as these coordinatively unsaturated sites exhibit strong hydrogen binding.[52] A reduction in these low-temperature desorption signals in spent samples is consistent with exchange of ligand centres with water/OH during the catalytic reaction.

At higher temperatures, exceeding 150 K, stronger interactions between hydrogen and the framework were evident. Notably, in both Pd-A and Pd-B spent samples, a pronounced HD desorption signal was detected around 250 K, which was significantly less pronounced in the reduced samples. This peak suggests particle growth during the catalytic reaction.[53] Even though TEM images (Fig. 2) indicated that there is no significant agglomeration, the possibility of slight particle growth cannot be excluded. Such subtle growth of Pd particles under catalytic conditions may lead to the creation of additional void

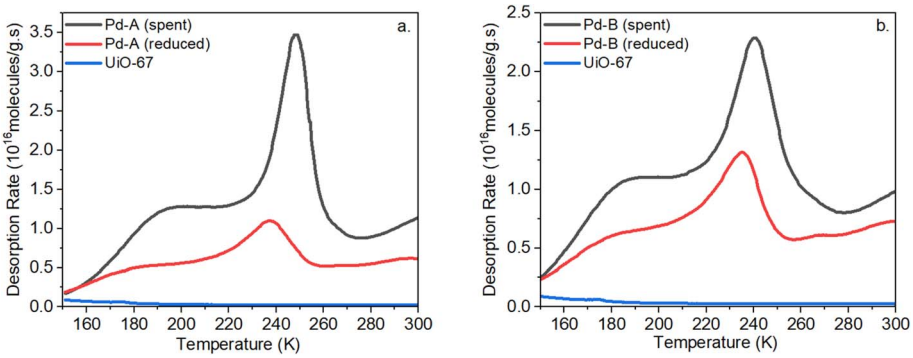

Fig. 5 Thermal desorption profile showing HD desorption at higher temperatures in (a) Pd-A spent and reduced samples, and (b) Pd-B spent and reduced samples, respectively.

space within the framework pores, potentially facilitating increased formation of interstitial hydrides. Since only metallic Pd can split H_2 and facilitate HD formation, the growth of Pd nanoparticles is further supported by the intense desorption peak observed in Pd-A spent, which is more prominent than in Pd-B spent. This indicates more significant Pd particle growth in the former under the tested catalytic conditions, aligning with the results obtained from EXAFS spectra.

Overall, *ex situ* XANES and EXAFS results emphasised the structural stability of the MOF framework and highlighted the dynamic nature of Pd species following catalytic processes. This underscores the importance of further investigation into the formation and evolution of these species throughout the catalytic cycle. To gain deeper insights into the behaviour of Pd species during the CO_2 hydrogenation to methanol, *ex situ* XAS and XRD experiments were performed on both Pd-A and Pd-B samples. These experiments aimed to elucidate the dynamic changes in the oxidation state and coordination environment of the Pd species under reaction conditions.

In situ XAS and XRD characterisations

In situ characterisations were conducted under 20 bar pressure, with the temperature varied between RT, 170 °C, and 240 °C following the reaction protocol depicted in Scheme S11. Although the primary objective of the study was to investigate the material under laboratory reaction conditions (170 °C during reduction and under the defined reactant gas composition), additional data was also collected at 240 °C under identical reactant-gas conditions to provide further insights into the materials' behaviour. During these experiments, XAS spectra, as well as XRD patterns, were collected quasi-simultaneously. These measurements aimed to provide detailed insights into the structural and electronic changes occurring within the catalysts under reaction conditions, offering a comprehensive understanding of the catalytic process at different temperatures.

Pd K-edge XANES and FT-EXAFS spectra collected during the experimental procedure for both Pd-A and Pd-B are presented in Fig. 6a and b, respectively. For clarity, only the most relevant experimental steps are shown. The spectra demonstrated nearly complete reduction to metallic Pd upon the introduction of H_2 into the system. Additionally, a progressive formation of Pd nanoparticles was observed, as evidenced by the enhancement of the corresponding spectral features during the reaction phase.

MCR-ALS analysis of the *in situ* XANES spectra (Fig. 6c, d, and S19) revealed a lower onset temperature for the Pd^{2+}-to-Pd^0 reduction in the Pd-B sample compared to Pd-A. However, above 175 °C, the extent of reduction became comparable between the two samples. Notably, the spectrum identified by the MCR-ALS routine as the Pd^{2+} component exhibited a broad white-line similar to that of Pd(II) acetate, along with a shoulder in the rising edge seen in PdO but not in Pd(II) acetate (Fig. S20). This further confirmed that the initial Pd state resembled disordered PdO nanoclusters.

Additional insight from the FT-EXAFS analysis, focusing on specific stages of the experimental protocol (Fig. 6b), showed that during thermal treatment under H_2, both Pd-A and Pd-B exhibited a decrease in the first coordination shell, accompanied by an increase in the Pd–Pd signal. This was consistent with the reduction to Pd^0 observed in XANES and the subsequent formation of Pd nanoparticles, the effect previously observed in the *ex situ* analysis.

When exposed to reaction conditions (CO_2 & H_2) at 170 °C, the Pd^0/Pd^{2+} ratio (Fig. S21) remained relatively unchanged, while the intensity of the Pd–Pd peak in the FT-EXAFS spectrum increased compared to inert conditions. This likely indicated a higher coordination number within the Pd nanoparticles during the reaction. Notably, when comparing the two samples under these specific conditions, at similar Pd^0/Pd^{2+} ratio, the Pd–Pd peaks displayed slight differences in intensity, suggesting variations in particle size between the systems. Specifically, Pd-B exhibited smaller Pd nanoparticles, which correlated with enhanced accessibility to active sites within the MOF pores and impacted the system's overall reactivity and selectivity.

As the temperature was further raised to 240 °C, an additional increase in the Pd–Pd peak intensity was observed. Both samples showed equivalent intensities, indicating structural similarity and comparable nanoparticle sizes. This behaviour aligns with prior studies showing that higher temperatures

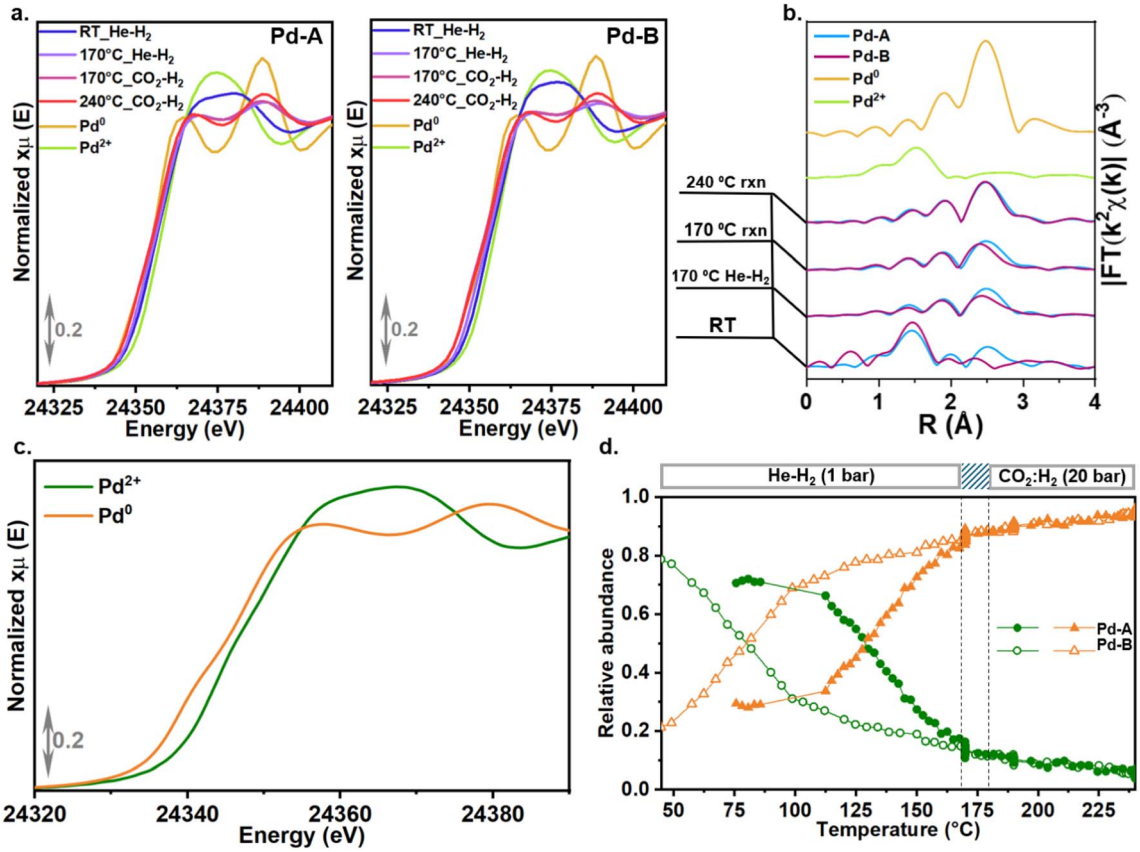

Fig. 6 (a) *In situ* Pd K-edge XANES spectra comparing between Pd-A (left) and Pd-B (right) samples collected in specific steps of the experiment, alongside spectra of relevant model compounds: Pd(II) acetate (Pd^{2+}) and Pd metal foil (Pd^0). (b) Phase-uncorrected magnitude component of FT-EXAFS spectra, obtained by Fourier transforming the $k^2\chi(k)$ curves in the 2.5–11.0 $Å^{-1}$ range. Experimental *k*-space EXAFS spectra are provided in Fig. S17. (c) Pd^0 and Pd^{2+} spectral components refined by MCR-ALS protocol. (d) Corresponding concentration profiles of Pd^0 and Pd^{2+} derived from MCR-ALS analysis (the light blue striped box is referring to the change in pressure from 1 bar to 20 bar during the $He–H_2$ gas feed). Experimental XANES spectra and residuals from MCR-ALS protocol are provided in Fig. S19.

promote sintering and particle growth in Pd-based catalysts, thereby influencing catalytic performance.[54,55]

Analysis of the Zr K-edge XANES spectra (Fig. 7a) revealed similarities with the *ex situ* spectra, consistent with Zr_6O_6 nodes in the UiO-67 structure. During the experiment, a slight decrease in the white-line intensity was observed, indicating a minor reduction in the average Zr coordination number, likely reflecting subtle structural changes. The FT-EXAFS spectra for

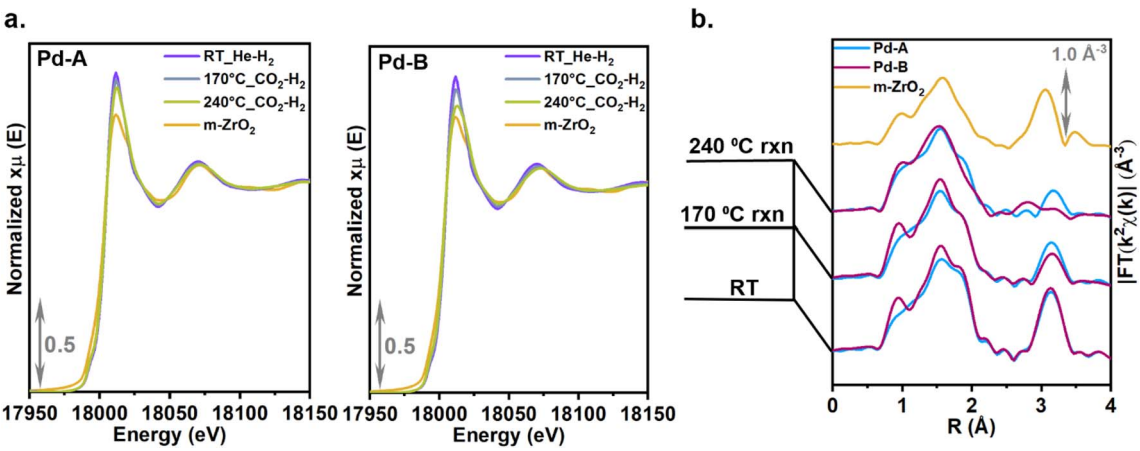

Fig. 7 (a) *In situ* Zr K-edge XANES spectra comparing between Pd-A (left) and Pd-B (right) samples collected at specific steps of the experiment; alongside the spectrum of a m-ZrO_2 reference sample for comparison. (b) Corresponding phase uncorrected magnitude component of FT-EXAFS spectra, obtained by Fourier transforming the $k^2\chi(k)$ curves in the 2.3–15.0 $Å^{-1}$ range.

both Pd-A and Pd-B samples (Fig. 7b) showed a decrease in the intensity of the Zr–Zr distance peak as the temperature increased to 170 °C. This was primarily attributed to higher thermal contributions to the Debye–Waller factors at elevated temperatures. However, minor differences between the samples suggest that the UiO-67 framework may have undergone local structural distortions influenced by the type and location of Pd species. These distortions appeared reversible, as no significant differences were observed between the *ex situ* spectra of the pristine and spent samples tested at 170 °C. This reversibility highlights the inherent flexibility of the UiO-67 framework, which accommodates temporary bond length and angle adjustments without compromising structural integrity, underscoring its robustness under moderate thermal conditions.

At 240 °C, more pronounced and potentially irreversible local distortions were observed. In particular, the Zr–Zr peak became indistinguishable in the Pd-B sample (Fig. 7b), indicating significant structural disruption under these harsher conditions. This absence suggests that Pd-B exhibited lower thermal stability compared to Pd-A, possibly due to differing interactions between Pd species and the UiO-67 framework. Despite such local distortions, the overall stability of the UiO-67 framework integrity in Pd-B was preserved overall, as confirmed by XRD analysis at 240 °C. This resilience underscores the robustness of the UiO-67 structure, even under demanding reaction conditions, and emphasises its potential as a durable catalyst support for high-temperature applications.

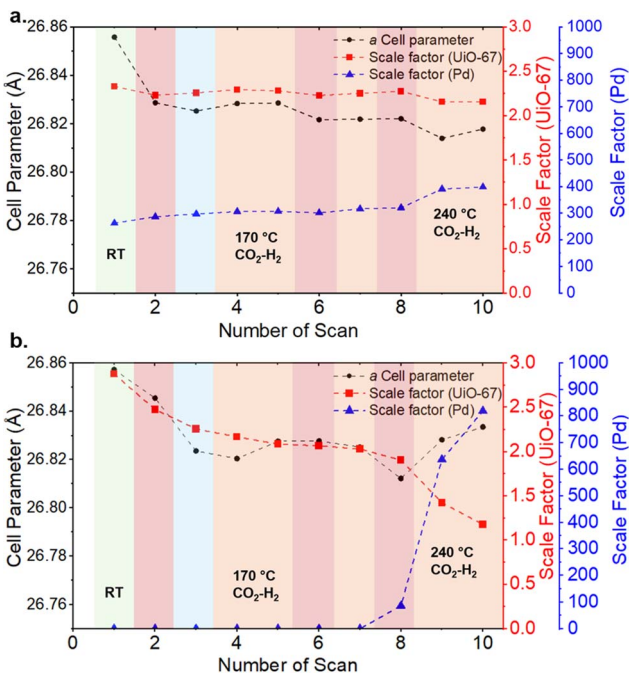

Fig. 8 Two-phase Rietveld refinement: Pd metal and UiO-67 for (a) Pd-A and (b) Pd-B catalysts at varying temperature. Green, red, blue, and orange areas correspond to room temperature, increasing temperature, activation, and reaction conditions, respectively, under which the measurements shown in the graph were performed.

Two-phase Rietveld refinement and PXRD analyses revealed distinct structural behaviours for the Pd-A and Pd-B samples under varying temperatures. For Pd-A, reflections corresponding to metallic palladium were already visible at room temperature (Fig. S22a), indicating the presence of nanoparticles large enough to be detected by XRD, consistent with the scale factor observed in Fig. 8. This observation aligns with the EXAFS spectra showing a Pd–Pd distance of approximately 2.5 Å (Fig. 3). Upon heating to 170 °C, no significant changes were observed in the Pd scale factor, whereas an increase at 240 °C suggested the formation of more well-ordered Pd^0 species. This behaviour indicates either the emergence of additional nanoparticles of sufficient size or the growth of existing ones through agglomeration. Notably, the UiO-67 scale factor remained stable, confirming that the MOF retained its crystallinity and structural integrity under these conditions.

In contrast, Pd-B exhibited no detectable reflections corresponding to metallic palladium at room temperature or 170 °C (Fig. S22b and 8), even though EXAFS spectra indicated the presence of small Pd clusters or nanoclusters. This discrepancy reflects the higher sensitivity of EXAFS toward small nanoparticles below the XRD detection limit. Upon heating to 240 °C (Fig. S22d), broad PXRD features characteristic of metallic Pd appeared, accompanied by a pronounced increase in the Pd scale factor. This was correlated with a decrease in the UiO-67 scale factor, suggesting partial loss of crystallinity due to Pd particle growth within the MOF pores, likely disrupting some linker–node bonds. Although the UiO-67 framework did not fully decompose, partial degradation was evident (Fig. S22). It should be noted that background parameters are strongly correlated with the Pd phase, especially for very small clusters, which limits the precision of quantitative XRD analysis. Therefore, a semi-qualitative evaluation of scale factor evolution was employed (Fig. 8) to interpret the temperature-dependent behaviour of both catalysts.

Conclusions

This study investigates the influence of palladium species on the catalytic performance of UiO-67-based catalysts for CO_2 hydrogenation to methanol by coupling *in situ* characterisation techniques with catalytic testing. A comparative analysis of Pd-A and Pd-B samples reveals that Pd particle size and distribution play a critical role in determining catalytic efficiency. Pd-B, featuring smaller Pd clusters confined within the UiO-67 framework, exhibited higher CO_2 conversion and methanol yield. This enhanced performance is attributed to the increased surface area-to-volume ratio of the Pd clusters and favourable electronic interactions between the metal species and the MOF framework. These findings align with literature reports suggesting that metal clusters confined within MOFs can offer superior catalytic activity due to greater accessibility of active sites and modified electronic properties. Notably, Pd-B exhibited superior methanol selectivity by suppressing methane formation, yielding CO as the sole by-product, and surpassing the performance of similar UiO-67-based catalysts reported in the literature. Furthermore, the study highlights the structural

robustness of UiO-67, which maintained its overall integrity despite local distortions at elevated temperatures. TEM analysis after prolonged reaction confirmed that the Pd-B catalyst maintains a highly dispersed nanoparticle distribution within the UiO-67 framework. This structural integrity under reaction conditions underscores the excellent thermal and chemical stability of the material, making it a promising candidate for sustained CO_2 hydrogenation to methanol. Overall, this work advances the understanding of structure–activity relationships in MOF-based catalysts and provides valuable guidance for the rational design of high-performance catalysts for CO_2 conversion. The results emphasise that precise control over the size and distribution of metal species within MOFs is crucial for maximising catalytic efficiency and selectivity in CO_2 hydrogenation.

Author contributions

E. T. synthesised and characterised the material, performed data analysis, participated in the synchrotron measurements, and wrote the first original draft. B. G. and D. S. joined the synchrotron measurements, analysed the XAS data, and significantly contributed to writing the manuscript. D. K. S. conducted the catalytic testing, helped with data analysis, and contributed to reviewing and editing the manuscript. I. C. B. joined the synchrotron measurements, analysed the *in situ* XRD data, and contributed to writing the manuscript. S. A. and P. S. performed the TDS measurements, with S. A. also contributing to manuscript writing. S. S., M. H., U. O., E. B., and P. A. S. contributed to reviewing and editing the manuscript, with P. A. S. additionally participating at the synchrotron measurements.

Conflicts of interest

The authors declare no competing financial interest.

Abbreviations

STP	standard temperature and pressure

Data availability

Supplementary information (SI): detailed synthetic protocols and characterisation protocols: MP-AES, TDS, detailed comparison of the as-prepared, Pd-loaded and post-catalysis samples with PXRD, BET, TGA, SEM, and TDS, as well as additional catalytic data. See DOI: https://doi.org/10.1039/d5ta05950j.

Acknowledgements

The authors would like to acknowledge the primary financial support provided by the Faculty of Mathematics and Natural Sciences through their Sustainable Development Initiative. S.A. also acknowledges funding from the University of Oslo (UiO). The authors express their gratitude to the European Synchrotron Radiation Facility (ESRF) for providing synchrotron radiation facilities under proposal number A31-1-206. Special thanks are extended to Dr Stoian Dragos and Dr Wouter van Beek for their invaluable assistance and support at beamline BM31. The BM31 setup was funded by the Swiss National Science Foundation (grant 206021_189629) and the Research Council of Norway (grant 296087). B. G. and E. B. acknowledge support from Project CH4.0 under the MUR program "Dipartimenti di Eccellenza 2023–2027" (CUP: D13C22003520001). E.T. acknowledges the valuable support of Christopher Affolter and Dr Erlend Aunan in the synthesis and characterisation of UiO-67, and of Rafael Cortez Sgroi Pupo for his guidance in NMR analysis. Also, authors would like to thank to Agnieszka Seremak for TOC of the manuscript. Finally, the authors acknowledge Dr Gabriel Antoine Alexandre Jeantelot for his contributions to the beamline campaign at ESRF.

References

1 S. Bilgen, *Renewable Sustainable Energy Rev.*, 2014, **38**, 890–902.
2 H.-J. Ho, A. Iizuka and E. Shibata, *Ind. Eng. Chem. Res.*, 2019, **58**, 8941–8954.
3 G. Wang, J. Chen, Y. Ding, P. Cai, L. Yi, Y. Li, C. Tu, Y. Hou, Z. Wen and L. Dai, *Chem. Soc. Rev.*, 2021, **50**, 4993–5061.
4 B. Hu, C. Guild and S. L. Suib, *J. CO_2 Util.*, 2013, **1**, 18–27.
5 A. Galadima and O. Muraza, *Renewable Sustainable Energy Rev.*, 2019, **115**, 109333.
6 G. A. Olah, A. Goeppert, G. K. S. Prakash, *Beyond Oil and Gas: The Methanol Economy*, 2009, pp. 233–278, DOI: 10.1002/9783527627806.ch12.
7 A. M. El-Zeftawy, *J. King Saud Univ., Eng. Sci.*, 1995, **7**, 209–254.
8 T. Sakakura, J.-C. Choi and H. Yasuda, *Chem. Rev.*, 2007, **107**, 2365–2387.
9 K. Stangeland, H. Li and Z. Yu, *Ind. Eng. Chem. Res.*, 2018, **57**, 4081–4094.
10 J. Gao, Y. Wang, Y. Ping, D. Hu, G. Xu, F. Gu and F. Su, *RSC Adv.*, 2012, **2**, 2358–2368.
11 M. Li, D. Li, M. O'Keeffe and O. M. Yaghi, *Chem. Rev.*, 2014, **114**, 1343–1370.
12 X.-J. Kong and J.-R. Li, *Engineering*, 2021, **7**, 1115–1139.
13 Z. Hu and D. Zhao, *CrystEngComm*, 2017, **19**, 4066–4081.
14 E. Tezel, D. K. Sannes, S. Svelle, P. Á. Szilágyi and U. Olsbye, *Mater. Adv.*, 2023, **4**, 5479–5495.
15 B. An, J. Zhang, K. Cheng, P. Ji, C. Wang and W. Lin, *J. Am. Chem. Soc.*, 2017, **139**, 3834–3840.
16 E. S. Gutterød, A. Lazzarini, T. Fjermestad, G. Kaur, M. Manzoli, S. Bordiga, S. Svelle, K. P. Lillerud, E. Skúlason, S. Øien-Ødegaard, A. Nova and U. Olsbye, *J. Am. Chem. Soc.*, 2020, **142**, 999–1009.
17 E. S. Gutterød, S. H. Pulumati, G. Kaur, A. Lazzarini, B. G. Solemsli, A. E. Gunnæs, C. Ahoba-Sam, M. E. Kalyva, J. A. Sannes, S. Svelle, E. Skúlason, A. Nova and U. Olsbye, *J. Am. Chem. Soc.*, 2020, **142**, 17105–17118.

18 A. A. Skorynina, A. Lazzarini, D. K. Sannes, E. G. Kozyr, C. Ahoba-Sam, S. Bordiga, U. Olsbye and A. L. Bugaev, *J. Mater. Chem. C*, 2024, **12**, 3564–3572.
19 E. S. Gutterød, S. Øien-Ødegaard, K. Bossers, A.-E. Nieuwelink, M. Manzoli, L. Braglia, A. Lazzarini, E. Borfecchia, S. Ahmadigoltapeh, B. Bouchevreau, B. T. Lønstad-Bleken, R. Henry, C. Lamberti, S. Bordiga, B. M. Weckhuysen, K. P. Lillerud and U. Olsbye, *Ind. Eng. Chem. Res.*, 2017, **56**, 13206–13218.
20 B. Panella, M. Hirscher and B. Ludescher, *Microporous Mesoporous Mater.*, 2007, **103**, 230–234.
21 B. G. Izar Capel Berdiell, G. Jeantelot, D. Salusso, P. Ágota Szilágyi and E. Tezel, *European Synchrotron Radiation Facility 2024*, 10.15151/ESRF-ES-1095654662.
22 B. Ravel and M. Newville, *J. Synchrotron Radiat.*, 2005, **12**, 537–541.
23 W. Windig, C. E. Heckler, F. A. Agblevor and R. J. Evans, *Chemom. Intell. Lab. Syst.*, 1992, **14**, 195–207.
24 J. Jaumot, R. Gargallo, A. de Juan and R. Tauler, *Chemom. Intell. Lab. Syst.*, 2005, **76**, 101–110.
25 S. Øien, D. Wragg, H. Reinsch, S. Svelle, S. Bordiga, C. Lamberti and K. P. Lillerud, *Cryst. Growth Des.*, 2014, **14**, 5370–5372.
26 J. H. Cavka, S. Jakobsen, U. Olsbye, N. Guillou, C. Lamberti, S. Bordiga and K. P. Lillerud, *J. Am. Chem. Soc.*, 2008, **130**, 13850–13851.
27 T. Toyao, K. Miyahara, M. Fujiwaki, T.-H. Kim, S. Dohshi, Y. Horiuchi and M. Matsuoka, *J. Phys. Chem. C*, 2015, **119**, 8131–8137.
28 D. K. Sannes, S. Øien-Ødegaard, E. Aunan, A. Nova and U. Olsbye, *Chem. Mater.*, 2023, **35**, 3793–3800.
29 Y. Zhu, J. Zheng, J. Ye, Y. Cui, K. Koh, L. Kovarik, D. M. Camaioni, J. L. Fulton, D. G. Truhlar, M. Neurock, C. J. Cramer, O. Y. Gutiérrez and J. A. Lercher, *Nat. Commun.*, 2020, **11**, 5849.
30 J. Zhang, B. An, Z. Li, Y. Cao, Y. Dai, W. Wang, L. Zeng, W. Lin and C. Wang, *J. Am. Chem. Soc.*, 2021, **143**, 8829–8837.
31 C. E. Pompe and P. Á. Szilágyi, *Faraday Discuss.*, 2021, **231**, 371–383.
32 J. Yu, G. Chen, Q. Guo, X. Guo, P. Da Costa and D. Mao, *Fuel*, 2022, **324**, 124694.
33 B. Rungtaweevoranit, J. Baek, J. R. Araujo, B. S. Archanjo, K. M. Choi, O. M. Yaghi and G. A. Somorjai, *Nano Lett.*, 2016, **16**, 7645–7649.
34 N. Lawes, I. E. Gow, L. R. Smith, K. J. Aggett, J. S. Hayward, L. Kabalan, A. J. Logsdail, T. J. A. Slater, M. Dearg, D. J. Morgan, N. F. Dummer, S. H. Taylor, M. Bowker, C. R. A. Catlow and G. J. Hutchings, *Faraday Discuss.*, 2023, **242**, 193–211.
35 C.-C. Hou, H.-F. Wang, C. Li and Q. Xu, *Energy Environ. Sci.*, 2020, **13**, 1658–1693.
36 J. K. Nørskov, T. Bligaard, B. Hvolbæk, F. Abild-Pedersen, I. Chorkendorff and C. H. Christensen, *Chem. Soc. Rev.*, 2008, **37**, 2163–2171.
37 H. Zhou, H. Jin, Y. Li, Y. Li, S. Huang, W. Lin, W. Chen and Y. Zhang, *Catalysts*, 2023, **13**, 1244.
38 S. Kaushal, G. Kaur, J. Kaur and P. P. Singh, *Mater. Adv.*, 2021, **2**, 7308–7335.
39 S. Pizzanelli, S. Monti, L. G. Gordeeva, M. V. Solovyeva, A. Freni and C. Forte, *Phys. Chem. Chem. Phys.*, 2020, **22**, 15222–15230.
40 L. Zhang, X. Liu, H. Wang, L. Cao, C. Huang, S. Li, X. Zhang, Q. Guan, X. Shao and J. Lu, *Catal. Sci. Technol.*, 2021, **11**, 4398–4405.
41 S. H. Pulumati, D. K. Sannes, C. R. Jabbour, L. D. B. Mandemaker, B. M. Weckhuysen, U. Olsbye, A. Nova and E. Skúlason, *ACS Catal.*, 2024, **14**, 382–394.
42 C. Ahoba-Sam, E. Borfecchia, A. Lazzarini, A. Bugaev, A. A. Isah, M. Taoufik, S. Bordiga and U. Olsbye, *Catal. Sci. Technol.*, 2020, **10**, 4373–4385.
43 A. Ramirez, P. Ticali, D. Salusso, T. Cordero-Lanzac, S. Ould-Chikh, C. Ahoba-Sam, A. L. Bugaev, E. Borfecchia, S. Morandi, M. Signorile, S. Bordiga, J. Gascon and U. Olsbye, *JACS Au*, 2021, **1**, 1719–1732.
44 V. V. Kaichev, A. A. Saraev, A. V. Fedorov and E. Y. Gerasimov, *Catalysts*, 2023, **13**, 1435.
45 J. Li, L. He, Q. Liu, Y. Ren and H. Jiang, *Nat. Commun.*, 2022, **13**, 928.
46 D. Salusso, E. Borfecchia and S. Bordiga, *J. Phys. Chem. C*, 2021, **125**, 22249–22261.
47 D. Salusso, P. Ticali, D. Stoian, S. Wang, W. Fan, S. Morandi, E. Borfecchia and S. Bordiga, *J. Phys. Chem. Lett.*, 2024, **15**, 4494–4500.
48 P. Li, I. W. Chen and J. E. Penner-Hahn, *Phys. Rev. B:Condens. Matter Mater. Phys.*, 1993, **48**, 10063–10073.
49 E. A. Redekop, T. Cordero-Lanzac, D. Salusso, A. Pokle, S. Oien-Odegaard, M. F. Sunding, S. Diplas, C. Negri, E. Borfecchia, S. Bordiga and U. Olsbye, *Chem. Mater.*, 2023, **35**, 10434–10445.
50 P. Ticali, D. Salusso, R. Ahmad, C. Ahoba-Sam, A. Ramirez, G. Shterk, K. A. Lomachenko, E. Borfecchia, S. Morandi, L. Cavallo, J. Gascon, S. Bordiga and U. Olsbye, *Catal. Sci. Technol.*, 2021, **11**, 1249–1268.
51 K. A. Lomachenko, J. Jacobsen, A. L. Bugaev, C. Atzori, F. Bonino, S. Bordiga, N. Stock and C. Lamberti, *J. Am. Chem. Soc.*, 2018, **140**, 17379–17383.
52 P. Á. Szilágyi, I. Weinrauch, H. Oh, M. Hirscher, J. Juan-Alcañiz, P. Serra-Crespo, M. de Respinis, B. J. Trześniewski, F. Kapteijn, H. Geerlings, J. Gascon, B. Dam, A. Grzech, R. van de Krol and H. Geerlings, *J. Phys. Chem. C*, 2014, **118**, 19572–19579.
53 J. King, Z. Lin, F. Zanca, H. Luo, L. Zhang, P. Cullen, M. Danaie, M. Hirscher, S. Meloni, A. M. Elena and P. Á. Szilágyi, *Phys. Chem. Chem. Phys.*, 2024, **26**, 25021–25028.
54 E. G. Kamyshova, A. A. Skorynina, A. L. Bugaev, C. Lamberti and A. V. Soldatov, *Radiat. Phys. Chem.*, 2020, **175**, 108144.
55 A. L. Bugaev, A. A. Guda, K. A. Lomachenko, E. G. Kamyshova, M. A. Soldatov, G. Kaur, S. Øien-Ødegaard, L. Braglia, A. Lazzarini, M. Manzoli, S. Bordiga, U. Olsbye, K. P. Lillerud, A. V. Soldatov and C. Lamberti, *Faraday Discuss.*, 2018, **208**, 287–306.

